Materials Research Bulletin 46 (2011) 850–857

Contents lists available at ScienceDirect

Materials Research Bulletin

journal homepage: www.elsevier.com/locate/matresbu

Effect of synthesis conditions on the nanopowder properties of $Ce_{0.9}Zr_{0.1}O_2$

M.G. Zimicz [a], I.O. Fábregas [a], D.G. Lamas [a], S.A. Larrondo [b,*]

[a] CINSO (Centro de Investigaciones en Sólidos) CONICET-CITEFA J.B. de La Salle 4397, 1603 Villa Martelli, Pcia. de Buenos Aires, Argentina
[b] Laboratorio de Procesos Catalíticos, Departamento de Ingeniería Química, Facultad de Ingeniería, Universidad de Buenos Aires, Pabellón de Industrias, Ciudad Universitaria, 1428 Buenos Aires, Argentina

ARTICLE INFO

Article history:
Received 23 January 2010
Received in revised form 24 December 2010
Accepted 14 February 2011
Available online 18 February 2011

Keywords:
A. Ceramics
A. Nanostructures
A. Oxides
B. Chemical synthesis

ABSTRACT

In this work, the synthesis of nanocrystalline $Ce_{0.9}Zr_{0.1}O_2$ powders via the gel-combustion method, using different fuels, and following either stoichiometric or non-stoichiometric pH-controlled routes is investigated. The objective is to evaluate the effect of synthesis conditions on the textural and morphological properties, and the crystal structure of the synthesized materials. The solids were characterized by nitrogen physisorption, Scanning Electron Microscopy (SEM), X-ray powder diffraction (XPD), and Carbon–Hydrogen–Nitrogen Elemental Analysis (CHN).

All the powders exhibited nanometric crystallite size, fluorite-type structure and negligible carbon content. Synthesis conditions strongly affect the average crystallite size, the degree of agglomeration, the specific surface area and the pore volume. Our results indicate that, by controlling the synthesis conditions it is possible to obtain solids with custom-made morphological properties.

© 2011 Elsevier Ltd. All rights reserved.

1. Introduction

Ceria (CeO_2)–Zirconia (ZrO_2) mixed oxides are important constituents of many catalytic systems [1–3]. Likewise, they have mixed ion-electronic conductivity, which make them attractive to be used as electrocatalytic anode materials in Solid Oxide Fuel Cells (SOFCs) [4].

The $Ce_{0.9}Zr_{0.1}O_2$ mixed oxide has shown excellent performance as catalyst in the total oxidation of methane [5], and as support in Ni–$Ce_{0.9}Zr_{0.1}O_2$ catalysts in partial oxidation of methane [6]. For these catalytic applications, decreasing the particle size and enlarging surface areas increase the number of active sites exposed to the reactant gaseous phase. Besides, anode materials for SOFCs should also exhibit high specific surface areas and enough porosity to expand the three-boundary region where the electrocatalytic reaction takes place. These characteristics are expected to be improved by the use of nanopowders with low degree of agglomeration. Therefore, it is important to find synthesis routes to achieve these goals with simplicity and in a short period of preparation.

Ceria–zirconia solid solutions can be synthesized following conventional methods, such as sol–gel [7], co-precipitation [7], Pechini method [8], gel-combustion [9–13], spray-pyrolysis [10,14,15], and solvothermal synthesis [16]. Among these, the gel-combustion process is one of the cheapest and simplest [17]. The gel-combustion technique used in this study consists of the following two steps. The first one involves the evaporation of water and the gelling of the solution containing the metal nitrates and the fuel (an aminoacid). The second one involves a deeper drying process of the resulting viscous liquid till the beginning of a self-sustained combustion. The combustion process is produced by the exothermic redox reaction between nitrate ions and fuel molecules. The main characteristics of this technique are high combustion temperatures, high temperature gradients and rapid expulsion of gases (short reaction times), which lead to final products with smaller particle size, higher surface areas, lower agglomeration and higher purity and homogeneity [17].

Although Glycine is one of the most popular fuels, reports using other fuels can also be found in the literature. Nevertheless, aminoacids are preferred over other fuels because their molecules have a carboxylic acid group at one end and an amino group at the other, giving to the molecule a "zwitterionic" feature that plays an efficient role in the complexation of metal cations [17]. By changing the fuel and the fuel/oxidizer ratio, it is possible to modify the synthesis conditions leading to materials with custom-made properties for catalytic and SOFCs applications.

In this work, we report the synthesis of $Ce_{0.9}Zr_{0.1}O_2$ solid solution by the gel-combustion method via novel routes. Different α-aminoacids are tested as fuels. Discussion of the effect of synthesis conditions (fuel, fuel/metal-cation molar ratio and

* Corresponding author. Tel.: +54 11 45763240; fax: +54 11 45763241.
E-mail address: susana@di.fcen.uba.ar (S.A. Larrondo).

0025-5408/$ – see front matter © 2011 Elsevier Ltd. All rights reserved.
doi:10.1016/j.materresbull.2011.02.008

calcination temperature) on the final structural and morphological properties is also presented.

2. Experimental

2.1. Synthesis procedure

$Ce_{0.9}Zr_{0.1}O_2$ nanopowders were synthesized by the gel-combustion method using different α-aminoacids (Glycine, Alanine and Lysine) as fuels. We studied both stoichiometric routes using all these fuels, and pH-controlled non-stoichiometric routes using only Glycine with different fuel contents. The samples in all the stoichiometric synthesis are identified with the first letter of the α-aminoacid followed by letter "S". On the other hand, the samples in the non-stoichiometric pH-controlled Glycine-nitrate routes with Glycine/metal-cation molar ratios of 3/1, 4/1, 5/1, 6/1 and 8/1 are labelled G3, G4, G5, G6 and G8, respectively.

The stoichiometric combustions proceed in accordance with the following equations:

$$0.9Ce(NO_3)_3{\cdot}6H_2O + 0.1ZrO(NO_3)_2{\cdot}6H_2O + \phi Glycine(C_2H_5NO_2) \rightarrow Ce_{0.9}Zr_{0.1}O_2 + 2\phi CO_2(g)\uparrow + (1.45 + 1/2\phi)N_2(g)\uparrow + (6 + 5/2\phi)H_2O(g)\uparrow \quad \Delta H^\circ = -2553\,(kJ/mol) \quad (1)$$

$$0.9Ce(NO_3)_3{\cdot}6H_2O + 0.1ZrO(NO_3)_2{\cdot}6H_2O + \theta Lysine(C_6H_{14}N_2O_2) \rightarrow Ce_{0.9}Zr_{0.1}O_2 + 6\theta CO_2(g)\uparrow + (1.45 + \theta)N_2(g)\uparrow + (6 + 7\theta)H_2O(g)\uparrow \quad \Delta H^\circ = -2266\,(kJ/mol) \quad (2)$$

$$0.9Ce(NO_3)_3{\cdot}6H_2O + 0.1ZrO(NO_3)_2{\cdot}6H_2O + \varphi Alanine(C_3H_7NO_2) \rightarrow Ce_{0.9}Zr_{0.1}O_2 + 3\varphi CO_2(g)\uparrow + (1.45 + 1/2\varphi)N_2(g)\uparrow + (6 + 7/2\varphi)H_2O(g)\uparrow \quad \Delta H^\circ = -2510\,(kJ/mol) \quad (3)$$

The symbols ϕ, θ and φ in Eqs. (1)–(3), represent the α-aminoacid/cation molar ratios, which take the values 1.511 (68/45), 0.400 (40/100) and 0.906 (68/75), respectively. Eqs. (1)–(3) represent the redox reaction between nitrate anions and the aminoacid, which is converted into carbon dioxide, nitrogen and water [17]. The combustions are self-sustained and proceed even in pure N_2 atmospheres [18]. The standard reaction enthalpies were evaluated using the values of standard enthalpies of formation of reactants and products found in the literature [9,18–23]. The temperature was followed by a thermal imaging camera FLIR Thermacam PM695 since the beginning of the gelling process.

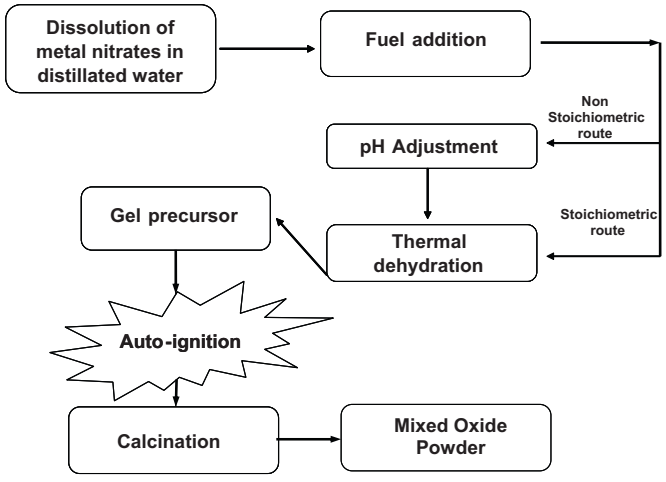

Fig. 1. Flow chart of the synthesis process.

A flow chart of the synthesis process is presented in Fig. 1. The differences between stoichiometric and non-stoichiometric routes are in the precursors used to obtain the gel. In the stoichiometric routes appropriate quantities of the raw salts, $Ce(NO_3)_3{\cdot}6H_2O$ (Alfa Aesar) and $ZrO(NO_3)_2{\cdot}6H_2O$ (Merck), and the aminoacid (all from Merck) are dissolved in the minimum volume of distilled water that leads to a limpid solution. In the non-stoichiometric routes $Ce(NO_3)_3{\cdot}6H_2O$ and $ZrOCl_2{\cdot}8H_2O$ are dissolved in distilled water, with 50 ml of nitric acid (65%, Merck) in a ratio corresponding to the desired final composition, and this solution is further concentrated by thermal evaporation in order to eliminate chloride anions. Glycine is added in the desired proportion of aminoacid/cation molar ratios and the pH of the solution is adjusted to pH 7 with ammonium hydroxide (25%, Merck).

In both cases, the solution obtained is heated on a hot plate at 280 °C to remove the water, getting a viscous gel that is finally self-burned, without observing inhomogeneous precipitation before the combustion.

After the combustion process, the obtained ashes were calcined in air at 600 °C for 2 h, in order to eliminate any vestige of carbonaceous residues. Due to the fact that nanoscale powders have higher sinterability than their microscale counterparts, some GS ashes were separated and calcined at 900 °C, to see the influence of calcination temperature on textural properties and morphology.

2.2. Characterization

2.2.1. Textural characterization

Nitrogen adsorption–desorption isotherms at 77 K were obtained for the three stoichiometric samples, GS, LS and AS, and for the sample GS calcined at 900 °C. For samples obtained via the non-stoichiometric route, only the Nitrogen adsorption isotherms were determined. The experiments were performed in a Micromeritics ASAP 2020 Accelerated Surface Area and Porosimetry Analyzer. Prior to the measurements, the samples were degassed at 250 °C for 7 h under vacuum (pressure < 20 μmHg).

2.2.2. Structural characterization

The structures of the solids were studied by X-ray Powder Diffraction techniques (XPD). The patterns were recorded with a Phillips PW3710 diffractometer using Cu Kα radiation, equipped with a graphite monochromator and operated at 40 kV and 30 mA. Data were collected in the 2θ = 20–100° region, with a step-size of 0.02° and a step-counting time of 12 s.

Rietveld refinements were performed for all XPD patterns using the Fullprof Suite software [24]. In these refinements, fluorite-type cubic structure was assumed: *Fm3m* space group, with Ce^{4+} and Zr^{4+} cations and O^{2-} anion in 4a and 8c positions, respectively. The peak shape was assumed to be a pseudo-Voigt function. The background of each profile was adjusted by a six-parameter polynomial function in $(2\theta)^n$, n = 0–5. Isotropic atomic temperature parameters were used. The thermal parameters corresponding to Ce^{4+} and Zr^{4+} cations were assumed to be equal.

The average crystallite size was calculated from the width of the (1 1 1) peaks using the Scherrer equation, $D_{XPD} = 0.9\lambda/\beta\cos(\theta)$ [25], where D_{XPD} is the crystallite size, λ is the radiation wavelength (1.5418 Å for Cu Kα radiation), β is the corrected peak width at half-maximum intensity and θ is the peak angular position. The value of β was corrected using the formula $\beta = \beta_m - \beta_i$, where β_m is the measured peak width, and β_i is the instrumental broadening determined with a LaB_6 standard.

2.2.3. Morphology of the samples

The morphology of the samples was examined by Scanning Electron Microscopy technique (SEM). The images were obtained with a Zeiss Electron Beam SEM-Supra 40. In order to avoid charging problems, the samples were placed over double-sided adhesive carbon-filled conductive ribbon. In some cases it was necessary to cover the sample with a gold film.

2.2.4. Analysis of the presence of carbonaceous residues

In order to detect the presence of carbonaceous residues after the calcination step, Carbon, Hydrogen and Nitrogen Elemental Analysis (CHN) experiments were carried out in a Carlo Erba Elemental Analyzer EA1108E1. The analytical method is based on the complete and instantaneous oxidation ("*flash combustion*") of a small portion of the sample, at high temperature. The effluent gases produced were analyzed with a chromatographic system with TCD detector. The detector was previously calibrated with a standard sample.

3. Results and discussion

3.1. Effect of process parameters in the auto-ignition of the gel-precursor

In the stoichiometric routes, a white-foam was formed, which experienced no volume increase before the beginning of the combustion. When Glycine and Alanine were used as fuels, the auto-ignition process began in the whole gel volume with a uniform distribution of the temperature (see Fig. 2a) and the complete combustion proceeded very fast. Powders obtained were voluminous, with uniform light yellow colour when observed with a standard bulb light (see Fig. 3). When Lysine was used as fuel, the auto-ignition process started with the development of a flame localized in a region, which slowly propagated throughout the viscous gel. Fewer quantities of evolved gases were observed in accordance with Eq. (2). The powder obtained was less voluminous with greyish-yellow colour when observed with a standard bulb light (see Fig. 3).

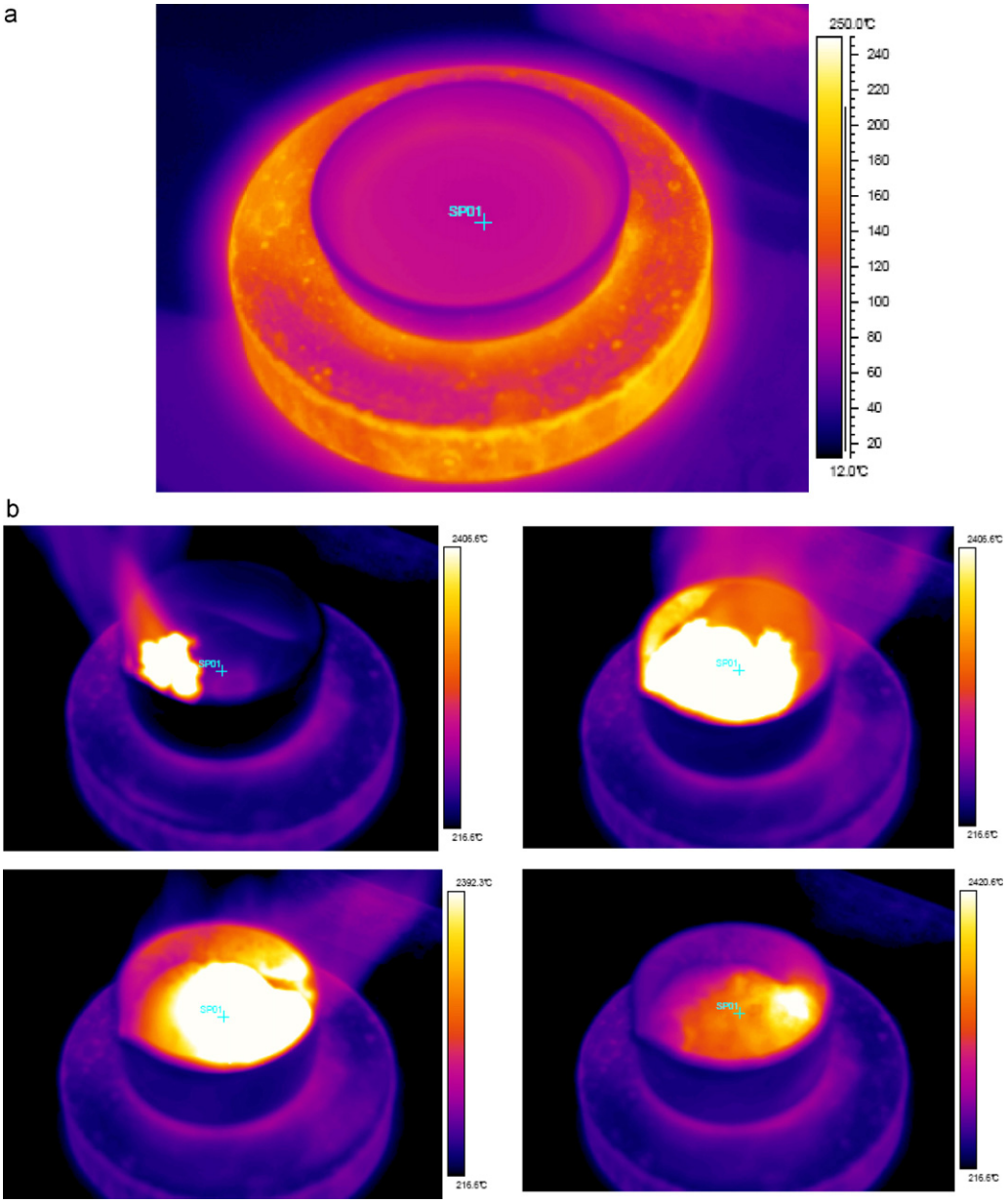

Fig. 2. Thermographic images of the combustion of (a) sample AS; (b) sample GN8.

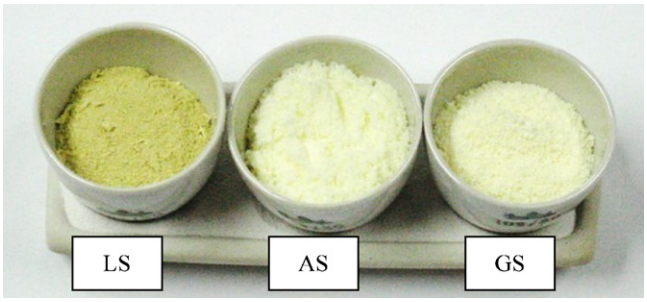

Fig. 3. Pictures of the samples obtained via the stoichiometric route with Lysine (LS), Alanine (AS) and Glycine (GS).

From Eqs. (1) to (3) it is possible to see that exothermic syntheses with Glycine and Alanine have similar standard enthalpies. The values are high enough to rise the temperature, favouring the combustion to occur. When Lysine is used as fuel the process is nearly 20% less exothermic. These differences in thermodynamic values and the kinetics of the combustion process affect the characteristics of the resulting powder.

In the non-stoichiometric pH-controlled Glycine-nitrate routes (samples G3–G8), the precursor gel had a large concentration of ammonium nitrate due to the incorporation of nitric acid and ammonium hydroxide [18]. Then, the reaction pathway was different from that proposed in Eqs. (1)–(3). A black-coloured foam was formed, which experienced an important volume increase before the developing of a flame. This black colour indicates the formation of carbonaceous compounds. The temperature was not uniform and the combustion process began in one region of the vessel and propagated to the rest of the volume exactly as a moving front as can be seen in Fig. 2b. The white area in the picture corresponds to the flame zone where the temperature is above 1500 °C (maximum temperature of the camera) producing a saturation effect. The increment in the Glycine/metal-cation molar ratio increased the amount of evolved gases and the rate of combustion of the gel. The powders obtained had a light yellow colour when observed with a standard bulb light.

3.2. Characterization results

The nitrogen adsorption–desorption isotherm for the sample GS calcined at 600 °C is depicted in Fig. 4. Similar adsorption–desorption curves were obtained for the samples AS and LS. The shape of the isotherms is intermediate between Types I and IV according to IUPAC classification [26], indicating the existence of micropores, mesopores and some macropores. Likewise, the nitrogen adsorption isotherm for samples G3, G4, G5, G6 and G8 are also intermediate between IUPAC Types I and IV. The results obtained from the analysis of isotherms are summarized in Tables 1a and 1b, for stoichiometric and non-stoichiometric routes, respectively.

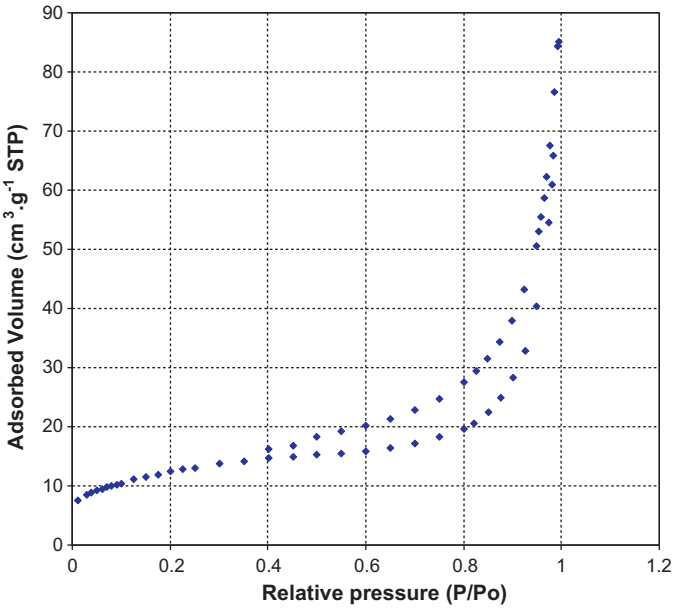

Fig. 4. N_2 adsorption–desorption isotherm for sample GS calcined at 600 °C.

In Table 1a, it is possible to see that there is a strong dependence of BET area and total pore volume with the fuel used in the synthesis process. For instance, the sample LS has very low BET area and pore volume, while the sample GS exhibits the highest values. This profound effect of the α-aminoacid used in the synthesis on the morphological characteristics of the samples can be observed in the SEM micrographs presented in Fig. 5. It is clear that samples GS and AS have a very porous structure, with the former presenting the largest pores, while the sample LS has a more compact structure. Another interesting point to analyse is the markedly difference in pore size distribution that can be observed in Fig. 5. Samples GS and AS have a broad distribution of pore sizes, while sample LS has more uniform pore diameters. These observations are in full agreement with the results obtained by applying the BJH model to adsorption and desorption branches of N_2 physisorption isotherm, which reveals the pore size distribution. The results are presented in Fig. 6. The samples GS and AS show a broad distribution of pore sizes in the 5–100 nm range, with a maximum around 10 nm. On the other hand, sample LS shows a narrow distribution of pores at 3.6 nm but only in the

Table 1a
Comparison of the main characteristics obtained from N_2 adsorption–desorption isotherms of samples GS (calcined at 600 °C an 900 °C), AS and LS (calcined at 600 °C).

	GS (900 °C)	GS (600 °C)	AS (600 °C)	LS (600 °C)
BET surface area ($m^2 g^{-1}$)	29 (1)	45 (2)	13.2 (7)	4.9 (3)
t-Plot external surface area ($m^2 g^{-1}$)	25 (1)	40 (2)	11.0 (6)	2.4 (1)
Total pore volume pores width < 50 nm ($cm^3 g^{-1}$)	0.085 (4)	0.086 (4)	0.028 (1)	0.011 (6)
t-Plot micropore volume ($cm^3 g^{-1}$)	0.0019 (4)	0.0013 (3)	0.0008 (2)	~0

Table 1b
Comparison of the main characteristics obtained from N_2 adsorption isotherms of samples G3, G4, G5, G6 and G8 calcined at 600 °C.

	G3	G4	G5	G6	G8
BET surface area ($m^2 g^{-1}$)	20 (1)	17 (1)	19 (1)	21 (1)	16 (1)
Total pore volume pores width <50 nm ($cm^3 g^{-1}$)	0.066 (3)	0.057 (3)	0.087 (4)	0.095 (5)	0.072 (4)
Adsorption average pore width (nm)	13	13	18	18	18

desorption branch. Then, the Tensile Strength Effect is affecting the desorption branch and is the responsible of these artificial pores at around 3.6 nm [27]. Nevertheless, it is clear that the pore volume is very low and distributed in the low pore-size range. As it can be observed from Eqs. (1) to (3), a larger length of the hydrocarbonated chain of the α-aminoacid produces lower volume of evolved gases and reduces the rate of the combustion, favouring the sintering of the crystallites in greater particles and the collapse of macro pores into micro pores, and leading to a reduction of the BET surface area, pore volume and pore width.

Comparing the textural properties of the sample GS calcined at 600 °C and 900 °C presented in Table 1a, it is possible to see that the increase in the calcination temperature reduces the BET area but does not modify the total pore volume. Besides, an increment in the micropore volume is observed. Then, the reduction of the BET area could be related to a sintering process of the particles, producing a collapse of macro pores.

It is possible to observe that a Glycine/metal-cation molar ratio higher than the stoichiometric value (Table 1b) reduces the BET area (16–20 $m^2\,g^{-1}$ against 44.6 $m^2\,g^{-1}$). The increment in the Glycine/metal-cation molar ratio is directly related with an increment of ammonium nitrate content in the precursor solution, which decomposes producing high quantities of evolved gases. This produces an increment in the total pore volume and the average pore width.

XPD patterns plotted in Figs. 7 and 8 show that all samples obtained after calcination at 600 °C exhibit the cubic fluorite-type crystal structure, corresponding to the spatial group *Fm3m*. No secondary phases or indications of compositional inhomogeneities were detected. The presence of broad peaks indicates that all solids have nanocrystalline nature. In Fig. 9, XPD patterns corresponding to the peak (1 1 1) for sample GS calcined at 600 °C and 900 °C are plotted. No phase segregation or any vestige of inhomogeneities was observed even in the sample calcined at 900 °C for 2 h. Besides, the increment in the calcination temperature increases the crystallite size as indicated by the narrower peak (1 1 1) in the XPD pattern (Fig. 9). The values of the lattice parameters obtained by Rietveld refinements, summarized in Table 2, are in good accordance to those reported in the literature [28]. In Fig. 11 the XPD patterns of the GS ashes obtained after gel combustion and the sample GS calcined at 600 °C are plotted. It is possible to observe that both patterns are similar, indicating that the mixed oxide is already formed before the calcination process. The crystallite sizes obtained by the Scherrer equation, presented in Table 2, were compared with the particle sizes calculated from the specific surface area $D_{BET} = 6/(\rho A)$, where ρ is the theoretical density of the material obtained from XPD analysis and A, the specific surface area obtained by the BET method. The degree of agglomeration, D_{BET}/D_{XPD}, is also informed in Table 2. It is worth to point out that in several samples we verified that the average particle size determined from SEM observations was very similar to D_{BET} (Fig. 10).

Stoichiometric routes resulted in average crystallite sizes considerably smaller than those obtained by non-stoichiometric

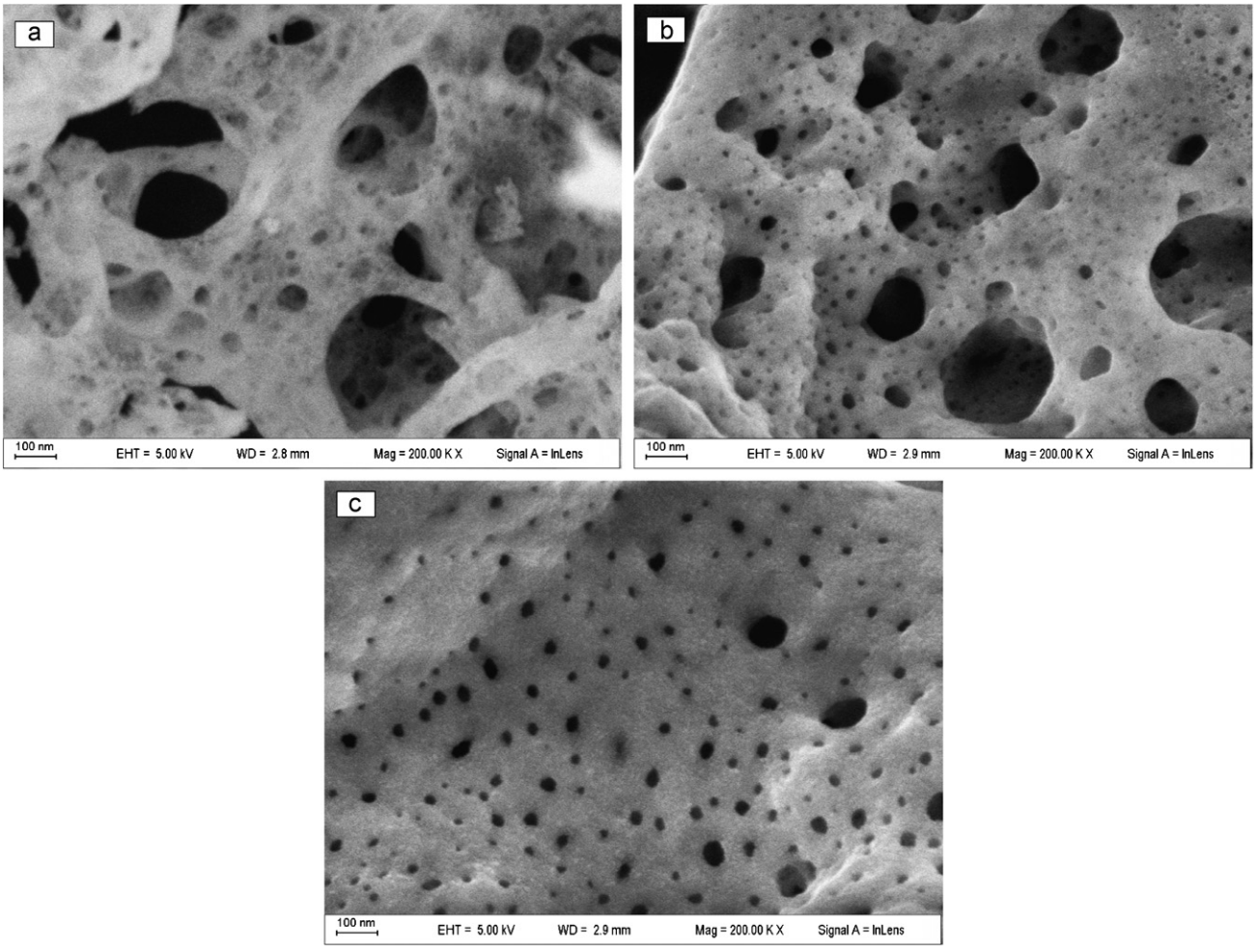

Fig. 5. SEM Micrographs for (a) GS, (b) AS, (c) LS samples calcined at 600 °C.

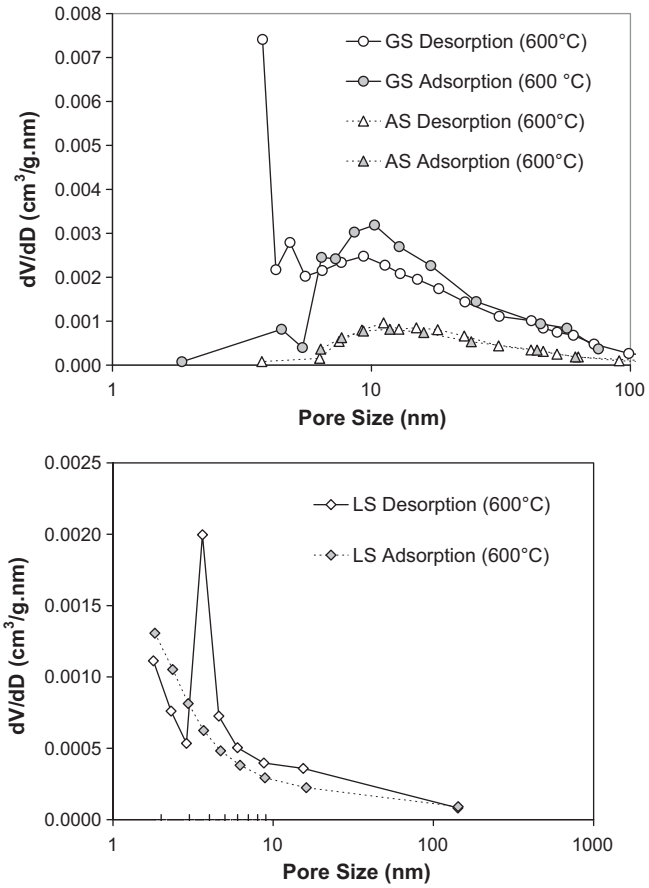

Fig. 6. Pore size distribution obtained with the BJH model.

synthesis. This is probably due to the fast kinetics of the combustion reaction of the gel precursor in stoichiometric routes. On the other hand, a greater degree of agglomeration was found in all the stoichiometric routes. The higher D_{BET}/D_{XPD} ratio could be related to the lower volume of evolved gases. For example, the sample synthesized with Lysine as fuel, following the stoichiometric route, with the lower volume of evolved gases, shows a high

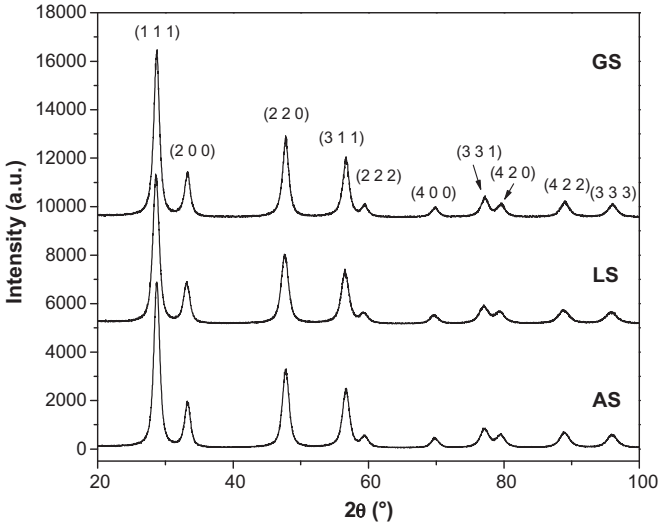

Fig. 7. XPD patterns for samples synthesized by stoichiometric routes with Glycine (GS), Lysine (LS) and Alanine (AS). Calcination temperature: 600 °C.

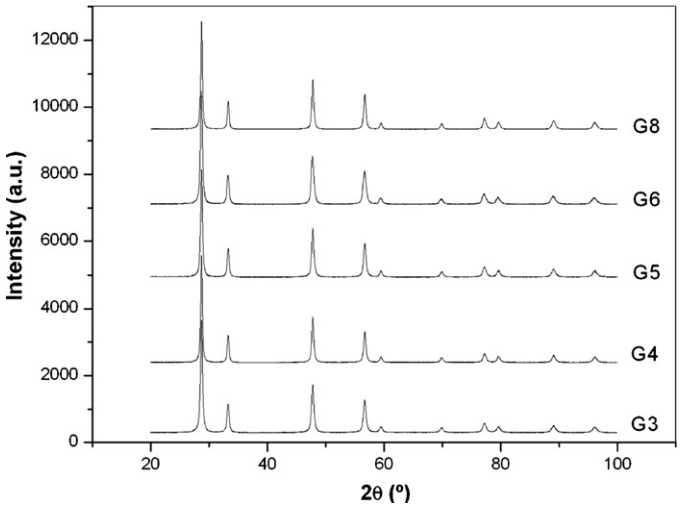

Fig. 8. XPD patterns for samples synthesized by non-stoichiometric routes with Glycine (G3, G4, G5, G6 and G8 correspond to Glycine/metal-cation molar ratios of 3/1, 4/1, 5/1, 6/1 and 8/1, respectively). Calcination temperature: 600 °C.

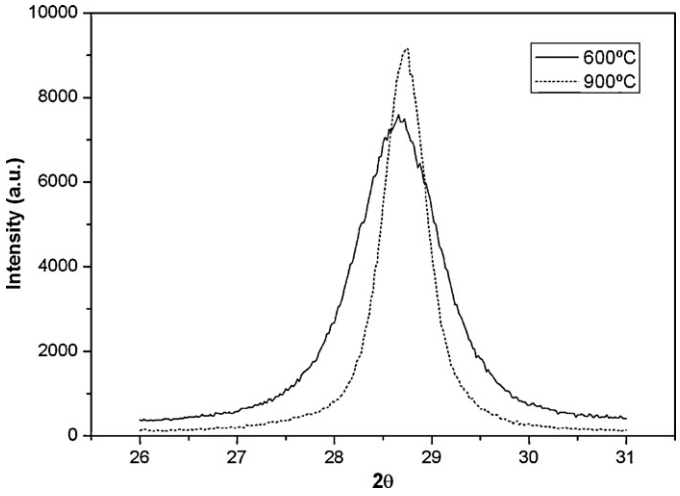

Fig. 9. XPD patterns for peak (1 1 1) region, for samples synthesized by stoichiometric combustion using Glycine as fuel, calcined at 600 °C and 900 °C.

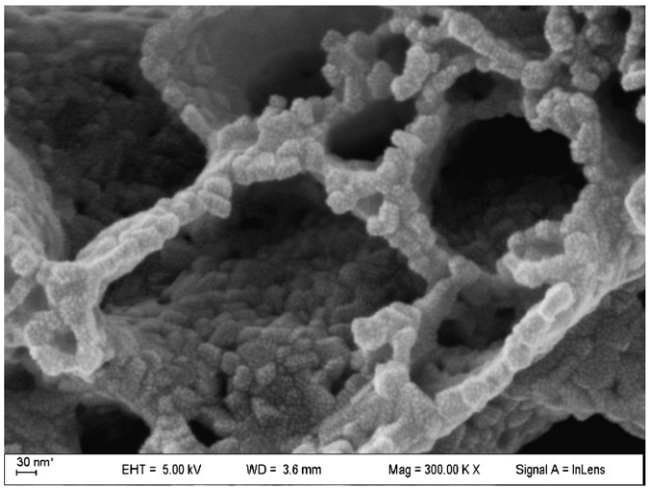

Fig. 10. SEM Micrography for sample G4 calcined at 600 °C.

Table 2
Lattice parameter (a) obtained by Rietveld refinement; average crystallite size (D_{XPD}) calculated by the Scherrer equation with peak (1 1 1); particle size calculated from specific surface area (D_{BET}); degree of agglomeration (D_{BET}/D_{XPD}).

Sample	T_{calc} = 600 °C				T_{calc} = 900 °C			
	a (Å)	D_{XPD} (nm)	$D_{BET} = 6/\rho S_g$ (nm)	D_{BET}/D_{XPD}	a (Å)	D_{XPD} (nm)	$D_{BET} = 6/\rho S_g$ (nm)	D_{BET}/D_{XPD}
GS	5.3883(8)	8.6(4)	19(1)	2.2(1)	5.3920(3)	18.6(9)	29(1)	1.5(1)
AS	5.3960(1)	8.6(3)	64(3)	7.4(3)	–	–	–	–
LS	5.3944(2)	7.9(4)	173(8)	22(1)	–	–	–	–
G3	5.3867(3)	27(2)	42(2)	1.5(1)	–	–	–	–
G4	5.3860(2)	35(2)	50(2)	1.4(1)	–	–	–	–
G5	5.3874(4)	29(2)	44(2)	1.5(1)	–	–	–	–
G6	5.3916(4)	26(2)	40(2)	1.5(1)	–	–	–	–
G8	5.3871(2)	35(2)	53(3)	1.5(1)	–	–	–	–

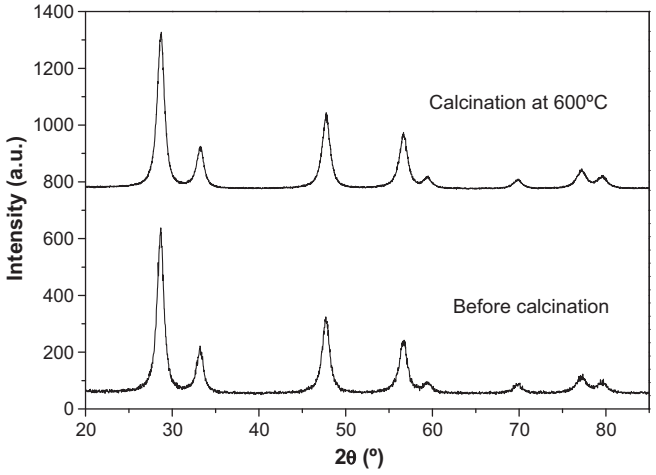

Fig. 11. XPD patterns for samples synthesized by stoichiometric combustion using Glycine as fuel, before and after calcination at 600 °C.

D_{BET}/D_{XPD} ratio, and very low pore volume. In the same sense, it can be observed in Table 2 that non-stoichiometric combustions, with higher mole number of evolved gases, have lower values of D_{BET}/D_{XPD} ratio. However, the temperature during the combustion reaction may also affect the agglomeration of the powders, since coarsening can be produced during this process. This is particularly relevant in the case of the non-stoichiometric pH-controlled routes.

CHN results showed that the calcination step efficiently removes combustion residues. The contents observed were: N <0.1% (m/m), C <0.2% (m/m) and H <0.3% (m/m).

4. Conclusions

The synthesis of ceria–zirconia solid solutions with nominal composition of $Ce_{0.9}Zr_{0.1}O_2$ by several gel-combustion routes is presented. The effect of α-aminoacid-to-metal molar ratio on the auto-ignition process and the powder characteristics has been explained.

All samples exhibited the fluorite-type crystal structure and nanometric average crystallite size.

For all routes, negligible carbon, nitrogen and hydrogen contents were observed after calcination, indicating that this treatment efficiently eliminates all the residual products formed during the gel-combustion process. Besides, most of the samples exhibited low degree of agglomeration.

From the point of view of the morphologic characteristics, it can be concluded that the stoichiometric routes should be preferred, because they produce solids with small average crystallite size, large specific surface area and big pore volume. Among the three fuels investigated in this work, Alanine, Lysine and Glycine, the last one leads to solids with the better morphologic characteristics for catalytic and SOFCs applications.

These results indicate that by controlling the synthesis conditions it is possible to obtain solids with tailored properties. Further research with other fuels and synthesis conditions will provide more insight in this subject.

Acknowledgements

The financial support from Agencia Nacional de Promoción Científica y Tecnológica-ANPCYT (PICT 2007-1152 and PAE-PICT 2007-02288), Fundación YPF (Estenssoro Fellowship), Universidad de Buenos Aires-UBA (UBACyT 2008-2010-I411) and CONICET (PIP No. 6559) is acknowledged.

References

[1] A. Trovarelli, M. Boaro, E. Rocchini, C. de Leitenburg, G. Dolcetti, J. Alloys Compd. 323–324 (2001) 584–591.
[2] P. Fornasiero, G. Balducci, R. Di Monte, J. Kaspar, V. Sergo, G. Gubitosa, A. Ferraro, M. Graziani, J. Catal. 164 (1996) 173–183.
[3] R. Di Monte, J. Kaspar, Catal. Today 100 (2005) 27–35.
[4] D.G. Lamas, M.D. Cabezas, I.O. Fábregas, N.E. Walsöe de Reca, G.E. Lascalea, A. Kodjaian, M.A. Vidal, N.E. Amadeo, S.A. Larrondo, ECS Trans. 7 (1) (2007) 961–970.
[5] S. Larrondo, M.A. Vidal, B. Irigoyen, A.F. Craievich, D.G. Lamas, I.O. Fábregas, et al. Catal. Today 107–108 (2005) 53–59.
[6] S.A. Larrondo, A. Kodjaian, I. Fábregas, M.G. Zimicz, N.E. Amadeo, N.E. Walsöe de Reca, D.G. Lamas, Int. J. Hydrogen Energy 33 (2008) 3607–3613.
[7] S. Rossignol, Y. Madier, D. Duprez, Catal. Today 50 (1999) 261–270.
[8] A.L. Quinelato, E. Longo, L.A. Perazolli, J.A. Varela, J. Eur. Ceram. Soc. 20 (2000) 1077–1084.
[9] S.T. Aruna, K.C. Patil, Nanostruct. Mater. 10 (1998) 955–964.
[10] D.G. Lamas, G.E. Lascalea, R.E. Juárez, E. Djurado, L. Pérez, N.E. Walsöe de Reca, J. Mater. Chem. 13 (2003) 904–910.
[11] G.E. Lascalea, D.G. Lamas, L. Pérez, E.D. Cabanillas, N.E. Walsöe de Reca, Mater. Lett. 58 (2004) 2456–2460.
[12] G.E. Lascalea, D.G. Lamas, E. Djurado, E.D. Cabanillas, N.E. Walsöe de Reca, Mater. Res. Bull. 40 (2005) 2029–2038.
[13] D.G. Lamas, R.O. Fuentes, I.O. Fábregas, M.E. Fernández de Rapp, G.E. Lascalea, J.R. Casanova, N.E. Walsöe de Reca, A.F. Craievich, J. Appl. Crystallogr. 38 (2005) 867–873.
[14] H.S. Kang, Y.C. Kang, H.Y. Koo, S.H. Ju, D.Y. Kim, S.K. Hong, J.R. Sohn, K.Y. Jung, S.B. Park, Mater. Sci. Eng. B 127 (2006) 99–104.
[15] S. Suda, M. Itagaki, E. Node, S. Takahashi, M. Kawano, H. Yoshida, T. Inagaki, J. Eur. Ceram. Soc. 26 (2006) 593–597.
[16] M.K. Devaraju, X. Liu, K. Yusuke, S. Yin, T. Sato, Nanotechnology 20 (2009) 405606.
[17] L.A. Chick, L.R. Pederson, G.D. Maupin, J.L. Bates, L.E. Thomas, G.J. Exarhos, Mater. Lett. 10 (1–2) (1990) 6–12.
[18] I.O. Fábregas, Ph.D. Thesis, Fases metaestables y nuevas propiedades de materiales nanoestructurados basados en ZrO_2, Aplicaciones en celdas de combustible de óxido sólido, University of Buenos Aires, Buenos Aires, Argentina, 2008 (in Spanish).
[19] X.W. Yang, J.R. Liua, S.L. Gaob, Y.D. Houb, Q.Z. Shib, Thermochim. Acta 329 (1999) 109–115.
[20] N.S. Jacobson, in: Thermodynamic Properties of Some Metal Oxide-Zirconia Systems, Technical Memo, National Aeronautics and Space Administration, Cleveland, OH, Lewis Research Centre, 1989.
[21] T.A. Lee, A. Navrotsky, I.J. Molodetsky, J. Mater. Res. 18 (4) (2003) 908–918.

[22] A. Navrotsky, P. Simoncic, H. Yokokawa, W. Chen, T. Lee, Faraday Discuss. 134 (2007) 171–180.
[23] C.D. Hodgman (Ed.), Handbook of Chemistry and Physics, Chemical Rubber Publishing Co., Cleveland, 1951.
[24] J. Rodríguez-Carvajal, Fullprof Suite 3.5d Version, 2005.
[25] H. Klug, L. Alexander, X-ray Diffraction Procedures for Polycrystalline and Amorphous Materials, John Wiley and Sons, 1974.
[26] F. Rouquerol, J. Rouquerol, K. Sing, Adsorption by Powders and Porous Solids, Academic Press, London, 1999.
[27] J.C. Groen, L.A.A. Peffer, J. Pérez-Ramírez, Micropor. Mesopor. Mater. 60 (2003) 1–17.
[28] R. Fornasiero, R. Di Monte, G. Ranga Rao, J. Kaspar, S. Meriani, A. Trovarelli, M. Graziani, J. Catal. 151 (1995) 168–177.